

# Mapping the Berry Curvature from Semiclassical Dynamics in Optical Lattices

H. M. Price and N. R. Cooper

*TCM Group, Cavendish Laboratory, J. J. Thomson Ave., Cambridge CB3 0HE, U.K.*

We propose a general method by which experiments on ultracold gases can be used to determine the topological properties of the energy bands of optical lattices, as represented by the map of the Berry curvature across the Brillouin zone. The Berry curvature modifies the semiclassical dynamics and hence the trajectory of a wavepacket undergoing Bloch oscillations. However, in two dimensions these trajectories may be complicated Lissajous-like figures, making it difficult to extract the effects of Berry curvature in general. We propose how this can instead be done using a “time-reversal” protocol. This compares the mean velocity of a wavepacket under positive and negative external force, and allows a clean measurement of the Berry curvature over the Brillouin zone. We discuss how this protocol may be implemented and explore the semiclassical dynamics for three specific systems: the asymmetric hexagonal lattice; and two “optical flux” lattices in which the Chern number is nonzero. Finally, we discuss general experimental considerations for observing Berry curvature effects in ultracold gases.

PACS numbers: 03.65.Sq, 03.65.Vf, 67.85.-d

## I. INTRODUCTION

One of the most interesting and surprising developments in the band theory of solids was the realization that the physical properties of any resulting energy band are not only encoded in its energy spectrum,  $\epsilon(\mathbf{k})$ , for all wavevectors  $\mathbf{k}$  in the Brillouin zone (the “bandstructure” in the usual sense). In addition, there are important physical consequences related to the topology of the *eigenstates* that form the band[1, 2].

The importance of topological features of the energy eigenstates was first pointed out in the seminal work of Thouless *et al.*[3] in the context of the integer quantum Hall effect. This work showed that, for two-dimensional (2D) lattices, the set of energy eigenstates that form an isolated band are characterized by an integer-valued Chern number,  $C$ , which can be nonzero when time-reversal symmetry is broken. The Chern number is a topological invariant of the band: its value cannot be changed by continuous evolution of the physical system without closing the gap to another band. Furthermore Ref. 3 showed that the Chern number has direct physical consequences: a filled band has a quantized Hall conductance equal to  $C$  times the quantum of conductance, corresponding to the existence of  $C$  chiral edge modes.

Soon after the work of Thouless *et al.*[3], the concept of the Berry phase was formulated[4]. The integer invariant of Ref. 3 was quickly interpreted[5] in terms of the integral of the Berry curvature in momentum space,  $\Omega(\mathbf{k})$ , over the Brillouin zone. This Berry curvature,  $\Omega(\mathbf{k})$  (defined below), is a gauge-invariant property of the bandstructure which is predicted to have direct physical consequences when the band is partially filled[6, 7]. A full description of the properties of an energy band therefore requires a specification of both the spectrum,  $\epsilon(\mathbf{k})$ , and the Berry curvature,  $\Omega(\mathbf{k})$ .

These considerations have become of immediate importance in the field of ultracold gases in optical lattices. While the Berry curvature vanishes for the simplest forms

of optical lattice, recent experiments have studied more complicated 2D optical lattices[8–10] for which simple variants exist in which the (local) Berry curvature is nonzero. Furthermore, there exist several theoretical proposals for forms of optical lattice in which the neutral atoms feel an effective magnetic field with high flux density[11–17]. These proposals are of great interest, as they offer the opportunity to study ultracold atoms in strong effective magnetic fields. These lattices break time-reversal symmetry in a way that leads to bands with non-zero Chern number [11, 15–17]. A key motivation of this work is to propose how the bandstructures of these lattices might be characterised experimentally. We shall focus on the “optical flux lattices” proposed in Refs. 16 and 17.

A particle picks up a Berry phase when it travels adiabatically around a closed contour. Here, we are concerned with contours in two-dimensional momentum space, with  $\mathbf{k}$  in the Brillouin zone. As usual, the Berry phase can be expressed as the integral of the Berry curvature,  $\Omega(\mathbf{k})$ , over the surface bounded by the contour. If the integral is over the entire Brillouin zone, the periodicity in  $\mathbf{k}$ -space means that the closed contour is equivalent to a point, and the Berry phase must be quantised as  $2\pi C$ , where  $C$  is the integer-valued Chern number. This is the topological invariant described above that underlies the remarkable quantisation of the quantum Hall effect [3, 18]. The Chern number has previously been measured through the conductance and chiral edge states of quantum Hall systems, and the total Berry phase associated with a Dirac point in graphene has been detected from transport[19, 20] and ARPES[21] measurements. To our knowledge, the local Berry curvature has never been measured directly, although its influence has been detected on a number of physical quantities [22]. It also plays an important role in the anomalous quantum Hall effect [7, 23, 24] and in semiclassical dynamics [6, 25, 26].

Ultracold gases present an excellent and unique opportunity to study the Chern number and the topology

of bands directly. Optical lattices can impose periodic potentials, and ultracold gas experiments are highly controllable, tunable and clean. Recent theoretical papers have shown how to detect the Chern number for certain tight binding models in time-of-flight measurements [27, 28]. In this paper, we propose a much more general method, based on semiclassical dynamics, that can be used to directly map out the Berry curvature over the Brillouin zone for any form of underlying lattice.

In the absence of Berry curvature, a wavepacket subjected to a constant external force will execute Bloch oscillations. These have not been observed for bulk crystalline electrons due to electronic scattering off lattice defects, but Bloch oscillations have been seen in other physical systems including semiconductor superlattices [29] and ultracold gases [30, 31].

In the presence of Berry curvature, the wavepacket dynamics will be strongly modified. In principle, these effects may be measured directly from the real-space trajectory of such a wavepacket, as has been previously proposed [32, 33]. However, in two dimensions, Bloch oscillations are complicated [34–36], and it can be difficult to disentangle the effects of Berry curvature from the usual effects arising from the group velocity. We propose how this may be overcome using a “time reversal” protocol. This will allow experiments to map the Berry curvature over the entire Brillouin zone for the first time.

The structure of the paper is the following. First, we introduce the Berry curvature and describe its effects on the semiclassical dynamics. We then discuss the complications of 2D Bloch oscillations and outline a protocol for how the Berry curvature may be mapped experimentally. We illustrate this discussion with numerical results for the Berry curvature and semiclassical dynamics for three interesting specific models: the asymmetric honeycomb lattice and two optical flux lattices [16, 17]. Finally we discuss general experimental considerations and time-of-flight experiments.

## II. THE BERRY CURVATURE AND SEMICLASSICAL DYNAMICS

From Bloch’s theorem, the eigenfunctions of a periodic potential can be expressed as  $\psi_{n,\mathbf{k}}(\mathbf{r}) = u_{n,\mathbf{k}}(\mathbf{r})e^{i\mathbf{k}\cdot\mathbf{r}}$ , where the Bloch function,  $u_{n,\mathbf{k}}(\mathbf{r})$ , has the periodicity of the underlying lattice and  $n$  is the band index. We confine our discussion to the 2D  $xy$  plane, where the bandstructure is characterised by the energy,  $\varepsilon_n(\mathbf{k})$ , and the scalar Berry curvature,  $\Omega_n(\mathbf{k})$ . All the concepts can be extended to three dimensions, where the Berry curvature must be treated vectorially.

The Berry phase,  $\gamma_n$ , for adiabatic transport in  $\mathbf{k}$ -space around a closed curve  $\mathcal{C}$  bounding a region  $\mathcal{S}$  is:

$$\gamma_n = \int_{\mathcal{C}} d\mathbf{k} \cdot \mathbf{A}_n(\mathbf{k}) = \int_{\mathcal{S}} d\mathbf{S} \cdot \hat{\mathbf{z}}\Omega_n(\mathbf{k}), \quad (1)$$

$$\mathbf{A}_n(\mathbf{k}) \equiv i\langle u_{n,\mathbf{k}}(\mathbf{r}) | \frac{\partial}{\partial \mathbf{k}} | u_{n,\mathbf{k}}(\mathbf{r}) \rangle, \quad (2)$$

$$\Omega_n(\mathbf{k}) \equiv \nabla_{\mathbf{k}} \times \mathbf{A}_n(\mathbf{k}) \cdot \hat{\mathbf{z}}, \quad (3)$$

where  $\mathbf{A}_n(\mathbf{k})$  is the Berry connection, a gauge dependent vector potential, and  $\Omega_n(\mathbf{k})$  is the Berry curvature. The Berry curvature is a gauge-invariant, local property of the bandstructure. It vanishes when both time-reversal and inversion symmetries are present. The Berry phase is geometrical and similar to the Aharonov-Bohm phase, with the Berry curvature playing the role of a magnetic field. When integrated over the whole Brillouin zone, the resultant Berry phase is quantised and equal to  $2\pi$  times the Chern number. The Chern number is thus a global topological property of the band, and underlies phenomena such as the integer quantum Hall effect [3]. However, the local Berry curvature also has important physical consequences, for instance, on the semiclassical motion of a wavepacket [6, 22, 25, 26].

To describe the semiclassical dynamics, we consider a gas of non-interacting fermions or bosons that is prepared in a wavepacket with a centre of mass at position,  $\mathbf{r}_c$ , and momentum,  $\mathbf{k}_c$  [37]. We consider a constant external force,  $\mathbf{F}$ , which in a solid state system would usually be due to an electric field. However, ultracold gases are neutral, and this force instead may come from linearly accelerating the lattice [30, 38] or from gravity [31, 39–41]. It is assumed that the force is sufficiently small that the motion is adiabatic such that Landau-Zener tunnelling is negligible and the wavepacket remains in a single band; henceforward we drop the band subscript  $n$ . The semiclassical equations of motion are then [25]:

$$\dot{\mathbf{r}}_c = \frac{1}{\hbar} \frac{\partial \varepsilon(\mathbf{k}_c)}{\partial \mathbf{k}_c} - (\dot{\mathbf{k}}_c \times \hat{\mathbf{z}})\Omega(\mathbf{k}_c), \quad (4)$$

$$\hbar \dot{\mathbf{k}}_c = \mathbf{F}. \quad (5)$$

We shall refer to the first term in (4) as the group velocity and to the second as the Berry velocity. We note that these semiclassical equations are further modified if there is an external “magnetic” field [25] in addition to the external force  $\mathbf{F}$ . We shall not discuss this further here, assuming that any magnetic field has the periodicity of the lattice and is incorporated into the bandstructure through the (magnetic) Bloch states  $u_{\mathbf{k}}(\mathbf{r})$  (see Section VB). The effect of a magnetic field on Bloch oscillations has also been analysed directly from the tight-binding Hamiltonian in Refs. 42 and 43.

To theoretically simulate the semiclassical dynamics, we must be able to calculate the Berry curvature. In general, a simple analytic expression is not possible and the Berry curvature is calculated numerically. This requires a discretised version of (3), as eigenfunctions are found computationally over a grid in  $k$ -space. There is an inherent phase ambiguity in the Bloch states, and so a gauge must be chosen to calculate the Berry connection. The Berry curvature is gauge-invariant, and can be found on this grid by the method of Fukui *et al.* [44], which applies a geometrical formulation of topological charges in lattice gauge theory, where the Berry curvature is calculated from the winding of  $U(1)$  link variables around

each plaquette in the Brillouin zone. We have used this method throughout this work for the numerical calculations.

### III. 2D BLOCH OSCILLATIONS

The pioneering experiments on Bloch oscillations in ultracold gases were (quasi-)one dimensional [30, 31], and only recently has the extension to 2D been investigated [10]. In 2D, Bloch oscillations have various interesting features in their own right, even before the Berry curvature is considered.

One important consequence of dimensionality is that the real-space Bloch oscillations in 2D become Lissajous-like [34–36]. For separable potentials, 1D Bloch oscillations along the  $x$  and  $y$  axes are simply superposed. For an arbitrary force  $\mathbf{F} = (F_x, F_y)$ , the wavepacket’s motion is periodic along  $k_i$  with  $\tau_{Bi} = \hbar/|F_i|a$  (where  $i$  runs over  $x, y$ ). The ensuing motion depends on the ratio  $F_x : F_y$ . For nonseparable potentials, studies show that similar behaviour can be expected when the force applied is weak and Landau-Zener tunnelling is negligible [34, 35].

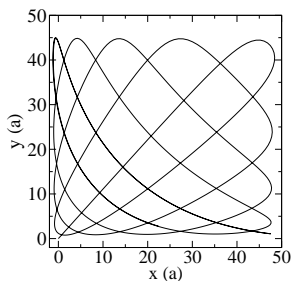


FIG. 1. An example of a Lissajous-like figure for the square optical flux lattice (Section VB 1). The ratio  $F_x : F_y$  is 9:10, and a low force of  $|\mathbf{F}| = 0.05F_R$  is used to minimise the effects of Berry curvature over one oscillation ( $F_R = \hbar^2/2m\lambda^3$  where  $\lambda$  is the optical wavelength and  $m$  is the mass of the atomic species, see Section V). The Lissajous-like figure is approximately bounded by the Bloch oscillation lengths, and so it obscures the effects of Berry curvature within this box.

The real-space Lissajous-like figures can be complicated two-dimensional oscillations, bounded by  $x_{Bi} \propto v_{Bi}\tau_{Bi}$  (Figure 1). For the Berry curvature to change this trajectory significantly, it would be necessary to wait until the wavepacket drifts outside of the bounding box. As a result, experiments would measure only the net Berry curvature encountered along a path. Information would be lost about how the Berry curvature is distributed in momentum space and notably whether its sign changes.

Furthermore, in 2D there can be an additional drift in the wavepacket’s position, independent of the Berry curvature, if the wavepacket doesn’t start at high symmetry points such as the zone centre  $\mathbf{k}_0 = (0, 0)$  [36, 45]. Thus, merely observing a transverse drift is not, by itself, conclusive evidence of nonzero Berry curvature.

### IV. A “TIME REVERSAL” PROTOCOL TO EXTRACT THE BERRY CURVATURE

Berry curvature effects can be isolated by considering the dynamics under a reversal of “time”. In doing so, it is important to be able to measure the velocity of the wavepacket. We shall discuss in Section VI how this may be done in experiments: for instance through tracking the position of the wavepacket in real space or through the momentum distribution, as in the seminal paper of Ben Dahan *et al.*[30].

We consider first measuring the velocity for a given force,  $\mathbf{F}$ , at a particular point,  $\mathbf{k}$ , in the Brillouin zone. This can be achieved in an experiment in which the wavepacket has evolved according to  $\mathbf{k}(t) = \mathbf{k}(0) + \mathbf{F}t/\hbar$ . This velocity is uniquely defined (within the single band approximation) at each point  $\mathbf{k}$  along the trajectory and we denote it as  $\mathbf{v}_{\mathbf{k}}(+\mathbf{F})$ . We now consider measuring the velocity in an experiment in which the wavepacket passes through the same point  $\mathbf{k}$ , but with opposite direction of the force,  $-\mathbf{F}$ , which we denote  $\mathbf{v}_{\mathbf{k}}(-\mathbf{F})$ . This can be achieved, for example, by evolving along the line  $\mathbf{k}(0) + \mathbf{F}t/\hbar$  for a time  $T$  that moves past the point of interest (e.g. to the Brillouin zone boundary), and then retracing this path using the reversed force  $-\mathbf{F}$ . From (4), we can see that the Berry velocity changes sign, while the group velocity remains invariant. The two effects can then be separated:

$$\mathbf{v}_{\mathbf{k}}(+\mathbf{F}) - \mathbf{v}_{\mathbf{k}}(-\mathbf{F}) = -\frac{2}{\hbar}(\mathbf{F} \times \hat{\mathbf{z}})\Omega(\mathbf{k}) \quad (6)$$

$$\mathbf{v}_{\mathbf{k}}(+\mathbf{F}) + \mathbf{v}_{\mathbf{k}}(-\mathbf{F}) = \frac{2}{\hbar} \frac{\partial \epsilon(\mathbf{k})}{\partial \mathbf{k}} \quad (7)$$

This transformation is equivalent to a time reversal operation, and it cleanly removes the effects of the complex Lissajous-like figures in 2D.

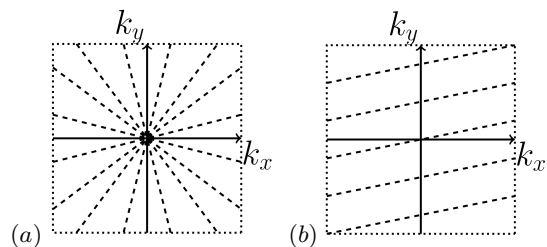


FIG. 2. Two methods for mapping the Brillouin zone. (a) Rotating the force with respect to the lattice between experiments allows each wavepacket to travel a different path. (b) With a large ratio  $F_x : F_y$ , a single wavepacket successively travels many paths within the Brillouin zone.

The Berry curvature can now be found at each point along the wavepacket’s path. By varying the path across the whole Brillouin zone, the Berry curvature is mapped out and the Chern number is directly measured. The path of the wavepacket may be chosen in various ways, two of which are illustrated in Figure 2. Firstly, the alignment of the force with the lattice may be rotated so that

different trajectories are successively explored. In such a scheme, the measurement time can be short, corresponding to the time taken for the wavepacket to travel once across the Brillouin zone. However, it would be important to align the force precisely each time. An alternative scheme would be to make the ratio  $F_x : F_y$  large. The wavepacket will cover a large area of the Brillouin zone during a single Bloch oscillation. The force needs to be aligned only twice (for  $+\mathbf{F}$  and  $-\mathbf{F}$ ) but longer measurement times would be required. A combination of these methods may be most suitable.

### A. Relation to the Chern Number

By this approach measurements of the velocity of the wave packet can be used to extract the Berry curvature. Measurements of the net drift of the wave packet in position space can be used to measure the Chern number of the band. To illustrate the idea, it is convenient to consider a BZ of rectangular symmetry, and the set of paths  $\mathbf{k} = (0, k_y) \rightarrow (K_x, k_y)$  that are traced out by a force  $+F$  in the  $x$ -direction, for different values of the initial wave vector  $k_y$ . Here  $K_x$  denotes the size of the reciprocal lattice vector in the  $x$  direction, so the path traverses the full width of the Brillouin zone once. The net drift of the wave packet in the  $y$  direction,  $\Delta y = \int v_y dt$ , is:

$$\Delta y(k_y, +F) = \int_0^{K_x} \frac{1}{F} \frac{\partial \epsilon}{\partial k_y} dk_x + \int_0^{K_x} \Omega(k_x, k_y) dk_x. \quad (8)$$

Note that, for general  $k_y$ , there is a transverse displacement not only from the Berry curvature but also from the group velocity[36, 45]. Reversing the force, such that the set of paths run in the opposite direction, over  $\mathbf{k} = (0, k_y) \rightarrow (-K_x, k_y)$ , the displacement becomes:

$$\Delta y(k_y, -F) = \int_0^{K_x} \frac{1}{F} \frac{\partial \epsilon}{\partial k_y} dk_x - \int_0^{K_x} \Omega(k_x, k_y) dk_x. \quad (9)$$

Thus, the contribution from the group velocity stays the same, but the contribution from the Berry curvature changes sign. Averaging the difference:

$$\frac{\Delta y(k_y, +F) - \Delta y(k_y, -F)}{2} = \int_0^{K_x} \Omega(k_x, k_y) dk_x \quad (10)$$

extracts the part that depends on the Berry curvature. It is interesting to note that this contribution is independent of the magnitude of the force. The size of the transverse displacement is just set by the length scale of the underlying lattice (the lattice constant), and a numerical factor that involves the average Berry curvature along the trajectory. Furthermore, the total Chern number can be found by summing over the set of trajectories with different values of  $k_y$ , which can be used to represent an evaluation of the integral:

$$C = \int_0^{K_y} dk_y \int_0^{K_x} dk_x \Omega(k_x, k_y) \quad (11)$$

at discrete points in  $k_y$ . (Clearly this approach can be readily adapted to a lattice of any symmetry, provided the set of paths spans the entire Brillouin zone once.)

## V. EXAMPLE SYSTEMS

In this section, we illustrate our proposed method for measuring the Berry curvature for three example systems that are of experimental interest: the asymmetric hexagonal lattice; and two optical flux lattices[16, 17] for which the Chern number is nonzero.

In optical lattices, the natural energy scale is set by the recoil energy,  $E_R = \hbar^2/2m\lambda^2$ , where  $\lambda$  is the optical wavelength. Similarly, we can define a recoil velocity,  $v_R = \hbar/m\lambda$ , and a unit of force,  $F_R = \hbar^2/2m\lambda^3$ . Hence forward, we express all quantities in these units.

The magnitude of the external force significantly affects the dynamics, as discussed further in Section VI. In previous experiments, the force has been introduced by linearly accelerating the lattice [30, 38], where the magnitude can be varied, or by gravity [31, 39–41]. In our units,  $|mg| = 0.7F_R$  for  $^{174}\text{Yb}$  and for  $\lambda = \lambda_0 \approx 578$  nm, the resonance wavelength coupling the ground and excited state in  $^{174}\text{Yb}$  [14]. This choice of parameters is especially relevant to the optical flux lattices discussed below. We therefore primarily focus on the representative case  $|\mathbf{F}| = 1F_R$ .

### A. The Asymmetric Hexagonal Lattice

The tight-binding hexagonal lattice has long been studied in condensed matter physics as a simple model for graphene [46]. Thanks to recent advances, optical lattices of hexagonal symmetry (or closely related forms) can be imposed on ultracold gases and phenomena associated with the interesting band topology can be directly studied [10, 47].

In the presence of both inversion and time-reversal symmetry, the bands touch at two Dirac points in the corners of the hexagonal Brillouin zone. If either of these symmetries is broken, band gaps open and Berry curvature appears at these points, as in the Haldane model where time reversal symmetry is broken [48]. The Chern number has also been observed experimentally for time-reversal symmetry breaking in graphene [19, 20].

The asymmetric hexagonal lattice instead breaks inversion symmetry by introducing an onsite energy difference between the two lattice sites,  $A$  and  $B$ . The opening of band gaps with asymmetry has already been studied experimentally in graphene[49], but Berry curvature effects have not been observed directly. Theoretically, the Berry curvature can lead to a quantum valley Hall effect, which may be useful for valley-based electronic applications [22, 46, 50]. It would therefore be of great interest to study this system in ultracold gases.

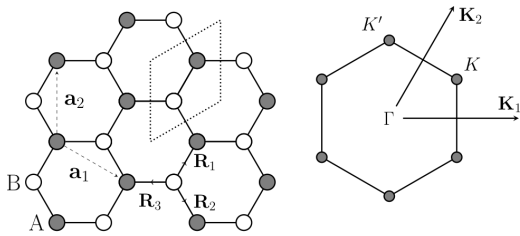


FIG. 3. The asymmetric hexagonal lattice in real space (on the left) and reciprocal space (on the right). The real space lattice vectors are  $\mathbf{a}_1 = a(\sqrt{3}/2, -1/2)$  and  $\mathbf{a}_2 = a(0, 1)$  where  $a$  is the lattice spacing (and for this geometry,  $a = 2\lambda/3$ ). The sublattices are connected by  $\mathbf{R}_1 = a(1/2\sqrt{3}, 1/2)$ ,  $\mathbf{R}_2 = a(1/2\sqrt{3}, -1/2)$  and  $\mathbf{R}_3 = a(-1/\sqrt{3}, 0)$ . The dotted lines indicate the unit cell. The reciprocal lattice vectors are then  $\mathbf{K}_1 = (4\pi/\sqrt{3}a)(1, 0)$  and  $\mathbf{K}_2 = (4\pi/\sqrt{3}a)(1/2, \sqrt{3}/2)$ .

The honeycomb lattice can be viewed as two interpenetrating triangular sublattices, for A and B, each with one site per unit cell (Figure 3). With onsite energies of  $\pm W$  on A/B sites, and including only nearest neighbour hoppings, the Hamiltonian is:

$$H(\mathbf{k}) = \begin{pmatrix} W & V(\mathbf{k}) \\ V^*(\mathbf{k}) & -W \end{pmatrix} \quad (12)$$

where  $V(\mathbf{k}) = -J[e^{i\mathbf{k}\cdot\mathbf{R}_1} + e^{i\mathbf{k}\cdot\mathbf{R}_2} + e^{i\mathbf{k}\cdot\mathbf{R}_3}]$ . The two energy bands are then:

$$\varepsilon(\mathbf{k}) = \pm\sqrt{W^2 + |V(\mathbf{k})|^2}. \quad (13)$$

For  $W = 0$ , the energy bands have two Dirac points at which  $|V(\mathbf{k})| = 0$ : these are at  $\mathbf{k} = (4\pi/\sqrt{3}a)(1/2, 1/2\sqrt{3})$  and  $\mathbf{k} = (4\pi/\sqrt{3}a)(0, 1/\sqrt{3})$  which we label as  $K$  and  $K'$ . Near each of the Dirac points, the effective Hamiltonian takes a simple form. Close to the Dirac point  $K$ , writing  $\mathbf{k} = (4\pi/\sqrt{3}a)(1/2, 1/2\sqrt{3}) + \mathbf{q}$ , the effective Hamiltonian is:

$$H(\mathbf{q}) = \begin{pmatrix} W & -\hbar v_F(q_x - iq_y) \\ -\hbar v_F(q_x + iq_y) & -W \end{pmatrix} \quad (14)$$

where  $\hbar v_F = (\sqrt{3}/2)aJ$ : a Dirac equation with mass. The Berry curvature can be found analytically near the Dirac point as [22]:

$$\Omega(\mathbf{q}) = \frac{\hbar^2 v_F^2 W}{2(W^2 + \hbar^2 v_F^2 q^2)^{3/2}} \quad (15)$$

For the Dirac point  $K'$ , writing  $\mathbf{k} = (4\pi/\sqrt{3}a)(0, 1/\sqrt{3}) + \mathbf{q}$ , the Berry curvature has the same form but opposite sign.

The resulting map of Berry curvature for the asymmetric hexagonal lattice is displayed in Figure 4(b). The Berry curvature around points  $K$  and  $K'$  has opposite signs such that the net Chern number of the band is zero. This vanishing Chern number is required by the fact that the system is time-reversal invariant.

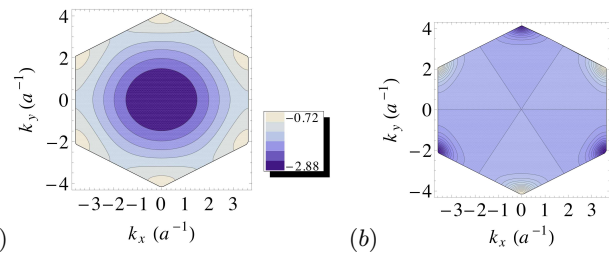


FIG. 4. (a) Bandstructure of the lowest band of the asymmetric hexagonal lattice for  $W = 0.5E_R$  and  $t = 1.0E_R$ , and the energy in units of  $E_R$  (for this geometry,  $a = 2\lambda/3$ ). Due to the asymmetry, gaps have opened at the Dirac points at the corners of the Brillouin zone. (b) The Berry curvature mapped out for  $W = 0.5E_R$ , using the method of Ref. 44. Light shading indicates  $\Omega > 0$  and dark shading indicates  $\Omega < 0$ . Positive and negative regions cancel, giving a net Chern number of zero.

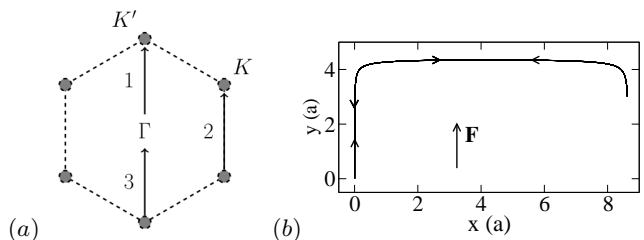


FIG. 5. (a) The trajectory of a semiclassical wavepacket through the Brillouin zone, starting from  $\mathbf{k} = (0, 0)$  with  $\mathbf{F} = (0, 0, 1.0F_R)$ . The numbers indicate the order in which the path is travelled. (b) The corresponding real-space trajectory of the wavepacket, starting from the origin, for  $W = 0.1E_R$ . This result was previously obtained in Ref. 33. The motion along  $x$  is due to the Berry curvature, while that along  $y$  is due to the bandstructure.

From the Berry curvature and bandstructure, we can now calculate the semiclassical motion of a wavepacket in this system (Figure 5). To illustrate clearly the effects of Berry curvature, we start the wavepacket at  $\mathbf{k} = (0, 0)$  and consider a force aligned along the  $y$ -direction, so that the 2D Bloch oscillation is also simply directed along  $y$ . This real space trajectory was previously obtained in Ref. 33, where the effects of a perturbing “magnetic” field were also discussed.

The velocities along  $x$  and  $y$  are shown in Figure 6. As the wavepacket passes through  $K'$ , the negative Berry curvature gives it a positive velocity in the  $x$  direction. In between  $K'$  and  $K$ , there is no curvature and it moves with a group velocity along  $y$ . When it passes through  $K$ , the positive curvature gives it negative  $x$  velocity. As the regions of curvature have the same magnitude, the effects cancel and there is no net drift.

For  $\mathbf{F} = (0, F)$  it is simple to determine the Berry curvature because the group and Berry velocities are perpendicular. For more general directions of the force, Lissajous-like oscillations will make it difficult to extract any information about the Berry curvature from the real

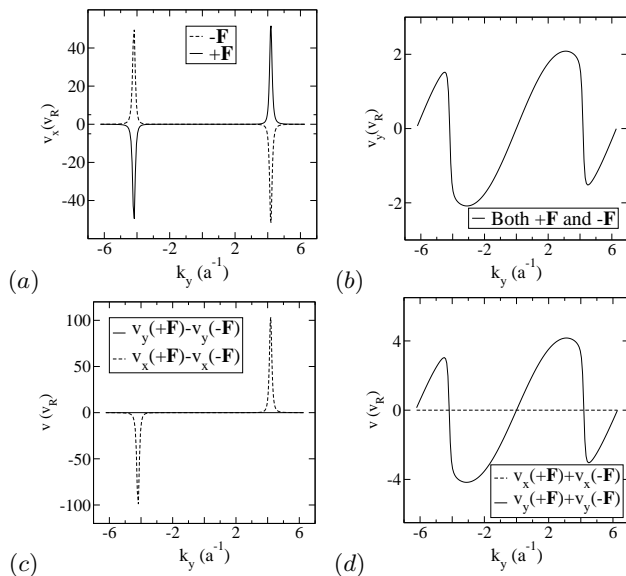


FIG. 6. (a) Velocity along  $x$  of a wavepacket moving under the force  $\mathbf{F} = \pm(0.0, 1.0E_R)$  with  $W = 0.1E_R$ .  $k_y$  is measured along the path travelled (which is periodic in  $4\pi$ ). (b) Velocity along  $y$ . (c) Applying the time-reversal protocol to extract the Berry velocity:  $\mathbf{v}(+\mathbf{F}) - \mathbf{v}(-\mathbf{F}) = -2/\hbar(\mathbf{F} \times \hat{\mathbf{z}})\Omega(\mathbf{k})$ . (d) Applying the time-reversal protocol to extract the group velocity:  $\mathbf{v}(+\mathbf{F}) + \mathbf{v}(-\mathbf{F}) = (2/\hbar)\partial\epsilon(\mathbf{k})/\partial\mathbf{k}$

space motion.

As proposed above, the Berry curvature may be cleanly mapped from the velocities using a time-reversal protocol. This is illustrated in Figure 6(c) and (d). Here the velocities along  $x$  and  $y$  for  $+\mathbf{F}$  and  $-\mathbf{F}$  are combined to show the Berry velocity and the group velocity respectively.

## B. Optical Flux Lattices

One of our main motivations for mapping the Berry curvature is to find a way of experimentally characterising optical flux lattices. These have lately been proposed as schemes to access fractional quantum Hall physics in ultracold gases [16, 17]. The optical flux lattices have bands with non-zero Chern number. They consist of a state dependent potential in register with an inter-species coupling, and lead to effective magnetic flux with a high non-zero average (with a non-zero integer number of magnetic flux quanta per unit cell). The specific optical coupling depends on the geometry and atomic species chosen. For atoms with a ground state and long-lived metastable excited state, such as an alkaline earth atom or ytterbium, a simple one-photon coupling scheme can be implemented [16]. For more commonly used atomic species, such as alkali atoms, two hyperfine states must be coupled via two photon processes [17]. Here, we discuss an example of each: the square one-photon optical

flux lattice and the  $F = 1/2$  two-photon optical flux lattice. The lowest energy band in both lattices can have a Chern number of one and hence is topologically equivalent to the lowest Landau level, allowing quantum Hall physics to be accessed.

### 1. One-Photon Square Optical Flux Lattice

In this scheme, the ground state and a long-lived excited state are coupled via a single photon [14]. The Hamiltonian in the rotating wave approximation is:

$$\hat{H} = \frac{\mathbf{p}^2}{2m} \hat{1} + \hat{V}(\mathbf{r}), \quad (16)$$

where  $\hat{1}$  and  $\hat{V}$  are  $2 \times 2$  matrices acting on the two internal states of the atom. We neglect interactions, an assumption that is discussed further in Section VI. The square optical flux lattice is generated when [16]:

$$\hat{V}_{sq} = V(\cos(\kappa x)\hat{\sigma}_x + \cos(\kappa y)\hat{\sigma}_y + \sin(\kappa x)\sin(\kappa y)\hat{\sigma}_z) \quad (17)$$

where  $V$  sets the energy scale of the potential,  $\kappa = 2\pi/a$  and the lattice vectors are  $\mathbf{a}_1 = (a, 0)$ ,  $\mathbf{a}_2 = (0, a)$ . The flux density is everywhere of the same sign, and leads to a total flux per unit cell of  $N_\phi = 2$  [16].

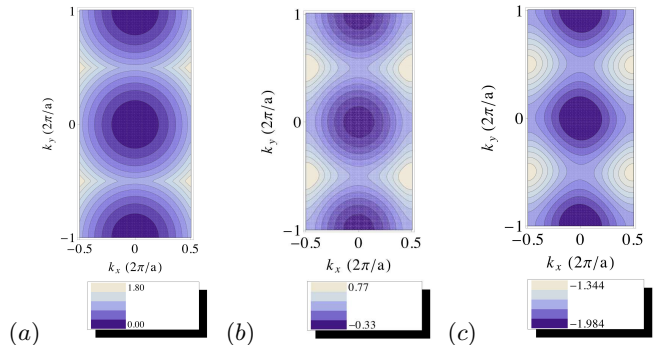


FIG. 7. Bandstructure of the lowest band in the magnetic Brillouin zone for the one-photon square optical flux lattice with (a)  $V = 0.0E_R$ , (b)  $V = 1.0E_R$  and (c)  $V = 3.0E_R$ , and the energy in units of  $E_R$ . At  $V = 0.0E_R$ , the lowest band touches the second lowest band at  $k = (\pi/a, \pm\pi/a)$ . As  $V$  is turned on, band gaps open at these points and Berry curvature is formed.

We consider the regime where  $V \lesssim \hbar^2\kappa^2/2m = 4E_R$  (for this geometry  $a = \lambda/2$ ). We expand the periodic Bloch functions over a set of reciprocal lattice vectors,  $\mathbf{K}$ :

$$u_{n,\mathbf{k}}(\mathbf{r}) = \frac{1}{\sqrt{N}} \sum_{\mathbf{K}} e^{-i\mathbf{K}\cdot\mathbf{r}} \begin{pmatrix} c_{\mathbf{K}}^{1(n,\mathbf{k})} \\ c_{\mathbf{K}}^{2(n,\mathbf{k})} \end{pmatrix} \quad (18)$$

and diagonalise the resulting Hamiltonian to find the bandstructure. As we consider low  $V$ , a small, finite set

of  $\mathbf{K}$  vectors will give the eigenfunctions and values to within the required numerical accuracy.

The eigenfunctions are everywhere two-fold degenerate, corresponding to two magnetic sub-bands. To distinguish between these states, we reinterpret the system within the magnetic Brillouin zone (MBZ) [16, 18, 25]. The optical coupling is invariant under the magnetic translation operators:

$$\hat{T}_1 \equiv \hat{\sigma}_y e^{\frac{1}{2}\mathbf{a}_1 \cdot \nabla} \quad \hat{T}_2 \equiv \hat{\sigma}_x e^{\frac{1}{2}\mathbf{a}_2 \cdot \nabla} \quad (19)$$

which do not commute but satisfy  $\hat{T}_2\hat{T}_1 = -\hat{T}_1\hat{T}_2$ . These operators represent rotations in spin space and translations by  $\frac{1}{2}\mathbf{a}_{1,2}$ , which enclose half a flux quantum (as  $N_\phi = 2$ ) [16, 18]. The magnetic Brillouin zone is defined by a unit cell containing an integer number of flux [18]; we choose a cell containing a single flux with vectors  $\mathbf{a}_1$  and  $\mathbf{a}_2/2$ . The corresponding commuting operators are  $\hat{T}_1^2$  and  $\hat{T}_2^2$ , with eigenvalues  $e^{i\mathbf{k} \cdot \mathbf{a}_1}$  and  $e^{i\mathbf{k} \cdot \mathbf{a}_2/2}$ . This defines the Bloch wavevector,  $\mathbf{k}$ , and the associated magnetic Brillouin zone [16]. Now the first Brillouin zone covers  $-\pi/a < k_x \leq \pi/a$  and  $-2\pi/a < k_y \leq 2\pi/a$ , doubling in size. Thanks to this unfolding, the lowest band is non-degenerate at each Bloch wavevector  $\mathbf{k}$ , and the resulting bandstructure is shown in Figure 7 for  $V = 0.0E_R$ ,  $V = 1.0E_R$  and  $V = 3.0E_R$ .

The Berry curvature is shown over the magnetic Brillouin zone for the lowest band in Figure 8, for  $V = 1.0E_R$  and  $V = 3.0E_R$ . For nonzero  $V$ , the Chern number of this band is one, so it is analogous to the lowest Landau level. For small  $V$  the Berry curvature,  $\Omega$ , is highly peaked at positions  $k = (\pi/a, \pm\pi/a)$ ; as  $V$  increases,  $\Omega$  spreads out while remaining centred on these two points.

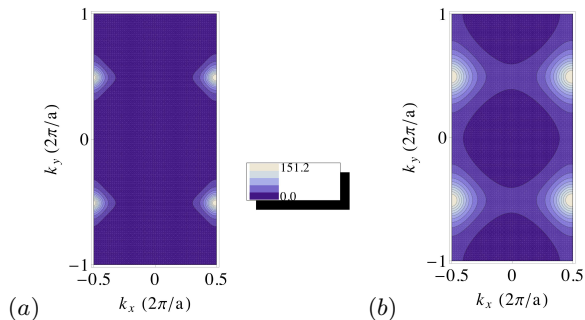


FIG. 8. Contour maps of the Berry curvature,  $\Omega(\mathbf{k})$ , for the square optical flux lattice when (a)  $V = 1.0E_R$  and (b)  $V = 3.0E_R$ .  $\Omega$  is in units of  $1/[\text{MBZ area}] = a^2/8\pi^2$ .  $\Omega$  is concentrated at points  $k = (\pi/a, \pm\pi/a)$ , spreading out with increasing  $V$ .

In Figure 9(b) we illustrate the real-space trajectory for semiclassical motion of a wavepacket in this optical flux lattice, for  $V = 0.4E_R$  and  $V = 2.0E_R$ . As discussed above, we focus on the case where  $|\mathbf{F}| = 1.0F_R$  which is representative of the gravitational force  $\mathbf{F} = m\mathbf{g}$  for  $^{174}\text{Yb}$  and  $\lambda = 578$  nm, parameters which are particularly relevant for this scheme [14, 16]. As shown in Figure 9(a), in momentum space the wavepacket starts

at  $\mathbf{k} = (0, 0)$  and moves under a force  $\mathbf{F}$  parallel to the  $(1, 1)$  direction such that it passes through the points  $\mathbf{k} = (\pi/a, \pm\pi/a)$  at which there is large positive Berry curvature. With  $\mathbf{F}$  aligned along  $(1, 1)$ , the group velocity is parallel to the force, while the Berry velocity is perpendicular (Figure 10). As the Berry curvature is everywhere positive, there is a net drift as successive regions of high  $\Omega$  are traversed. With higher  $V$ , the Berry curvature spreads out and hence the trajectory bends along more of its length. The dependence of the motion on  $V$  and  $|\mathbf{F}|$  is discussed in more detail in Section VI.

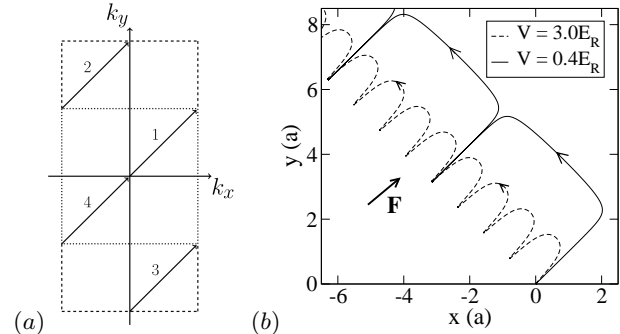


FIG. 9. (a) The trajectory of a semiclassical wavepacket through the magnetic Brillouin zone, starting from  $\mathbf{k} = (0, 0)$  with  $|\mathbf{F}| = 1.0F_R$  directed along  $(1, 1)$ . The numbers indicate the order in which the path is travelled. The dotted line indicates the simple Brillouin zone, while the dashed lines shows the extension into the magnetic Brillouin zone. (b) The corresponding real-space trajectory of the wavepacket starting from the origin, for  $V = 0.4E_R$  and  $V = 3.0E_R$ . The motion perpendicular to  $\mathbf{F}$  is due to the Berry curvature, while that parallel is due to the bandstructure.

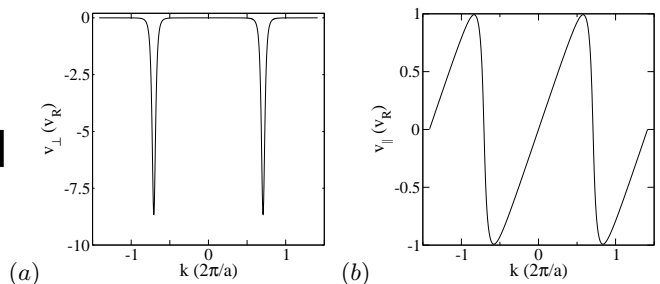


FIG. 10. The velocity of the wavepacket (a) perpendicular and (b) parallel to the applied force for  $|\mathbf{F}| = 1.0F_R$  directed along  $(1, 1)$  and  $V = 0.4E_R$ .  $k$  is measured along the path travelled. For this simple alignment of the force, (a) contains the effects of Berry curvature along the path, while (b) shows the group velocity.

As before, the simplicity of the trajectories and velocities relies on the alignment of  $\mathbf{F}$  along a special direction. More generally in 2D, the Bloch velocity will not be parallel to the force and complex Lissajous-like figures will be observed; an example of this was previously shown in Figure 1 for one oscillation at a low force,  $|\mathbf{F}| = 0.05F_R$ , where the effects of Berry curvature are small.

Here we demonstrate the effect of Lissajous-like figures on the motion for parameter ranges of interest. Figure 11 shows the real-space trajectories for (a)  $|\mathbf{F}| = 1.0F_R$  and (b)  $5.0F_R$ , when the force is aligned such that  $F_x : F_y = 1 : 16$ . The Bloch motion is no longer purely parallel to the force and while an average drift may be measured, the details of the motion due to Berry curvature have been lost.

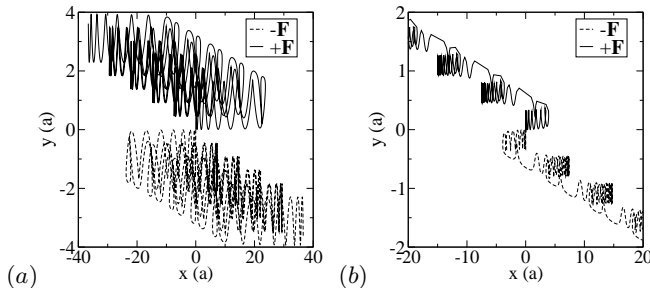


FIG. 11. Trajectory for a wavepacket travelling with (a)  $|\mathbf{F}| = 1.0F_R$  and (b)  $|\mathbf{F}| = 5.0F_R$  where the force is aligned such that  $F_x : F_y = 1 : 16$  and  $V = 0.4E_R$ . The Bloch motion is no longer purely along the direction of the force, and the resultant trajectory is complex. The net drift between Bloch oscillations is a measure of the total Berry curvature along a path, but other information is obscured. The trajectory due to the group velocity increases in size relative to the trajectory due to the Berry curvature with decreasing force (Section VI), leading to more complicated motion in (a) than (b).

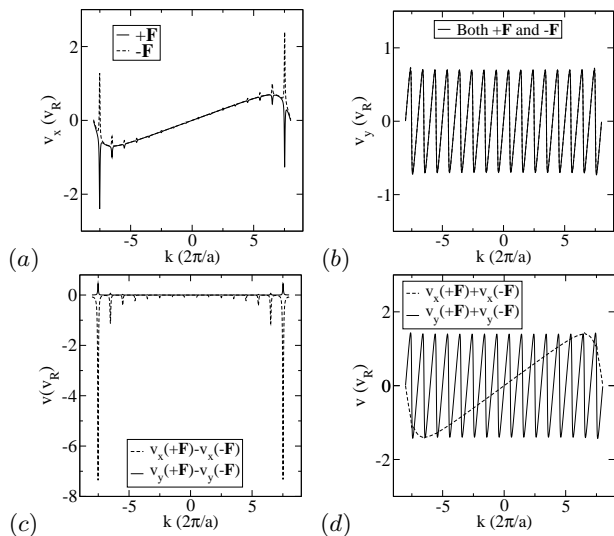


FIG. 12. (a) Velocity along  $x$  of a wavepacket moving under the force  $|\mathbf{F}| = 1.0F_R$  with  $F_x : F_y = 1 : 16$  and  $V = 0.4E_R$ .  $k$  is measured along the path travelled. (b) Velocity along  $y$ . (c) Applying the time-reversal protocol to extract the Berry velocity. The Berry velocity calculated from  $v_x$  and  $v_y$  differ by a factor of 16 from the ratio of the forces, and by a sign, due to the cross product. (d) Applying the time-reversal protocol to extract the group velocity. As expected, there are 16 oscillations from  $v_y$  for every one from  $v_x$ .

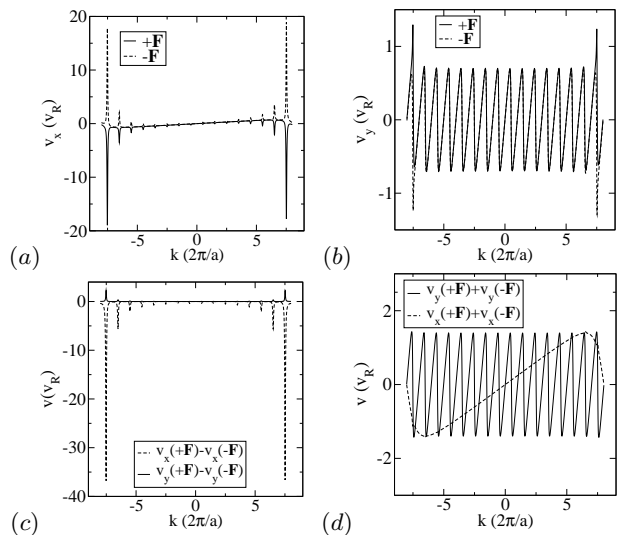


FIG. 13. As in Figure 12 but now for  $|\mathbf{F}| = 5.0F_R$ .

We illustrate how our time-reversal protocol may be used to extract the local Berry curvature. Figures 12 and 13 show the velocities along  $x$  and  $y$  over the path through the Brillouin zone. By comparing the time-reversed velocities, quantities proportional to the Berry velocity and the group velocity are extracted. Figure 14 shows the resulting map of Berry curvature over the Brillouin zone for  $|\mathbf{F}| = 1.0F_R$ , the same result being obtained (up to a scale factor) from either of these two cases of different magnitude of the force.

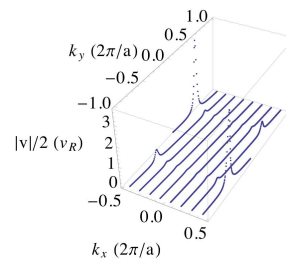


FIG. 14.  $|v_x(+\mathbf{F}) - v_x(-\mathbf{F})|/2 = 1/\hbar(F_y\Omega)$  plotted along the path taken by the wavepacket in the Brillouin zone for  $|\mathbf{F}| = 1.0F_R$  with  $F_x : F_y = 1 : 16$  and  $V = 0.4E_R$ . This technique will enable experiments to directly map out the Berry curvature.

## 2. Two-Photon Optical Flux Lattice for $F = 1/2$

To generate optical flux lattices for the more commonly used alkali atoms one must employ dressed states involving a two-photon coupling [17]. We consider the representative case of a lattice with triangular symmetry where the hyperfine states coupled have angular momentum  $F = 1/2$ , as in species like  $^{171}\text{Yb}$ . Qualitatively similar semiclassical dynamics are expected for other values

of  $F$ , such as the experimentally relevant case of  $F = 1$  for  $^{87}\text{Rb}$  [17]. The two-photon optical flux lattice we study leads to a net effective magnetic field in real space in which there is one flux quantum per unit cell. Semiclassical motion within a similar scheme has previously been studied in Ref. 32. In that scheme, the artificial magnetic field is still locally non zero, but the flux per unit cell vanishes [17, 32] and the Chern number of each band is zero. For the optical flux lattice described here, the energy bands may have non-zero Chern numbers.

For the  $F = 1/2$  optical flux lattice, two hyperfine ground states,  $g_{\pm}$ , with angular momentum  $J_g = 1/2$ , are coupled to an excited state,  $e$ , also with angular momentum  $J_e = 1/2$ , via an off-resonance excitation that ensures the population of  $e$  remains negligible. The Hamiltonian then acts in the  $g_{\pm}$  manifold, with the form of (16). The details of the optical coupling and the resulting Hamiltonian are discussed in Ref. [17] and in Appendix A.

The final Hamiltonian can be written as:

$$\hat{H}' = \hat{U}^\dagger \hat{H} \hat{U} = \frac{(\mathbf{p} - \hat{\sigma}_z \hbar \mathbf{k}_3/2)^2}{2m} + \hat{V}', \quad (20)$$

where  $\mathbf{k}_3 = k(0, 1, 0)$ , and  $\hat{U}$  is a unitary transformation that is applied to expose the full symmetry of the system. The transformed optical potential  $\hat{V}'$  has the maximal translational symmetry, causing  $\hat{\mathbf{p}}/\hbar$  to be conserved up to the addition of the reciprocal lattice vectors  $\mathbf{K}_{1/2} = -k/2(\pm\sqrt{3}, 3, 0)$  (Appendix A). The resulting Brillouin zone, defined by  $\mathbf{K}_{1/2}$ , is equivalent to the asymmetric hexagonal lattice in Section V A. As can be seen, an important feature of the two-photon optical flux lattice is that, under this unitary transformation, the momenta of  $g_{\pm}$  are offset by  $\pm\hbar\mathbf{k}_3/2$ . This offset does not affect the semiclassical equations of motion, which determine the rate of change of (crystal) momentum under an applied force (5), and which still apply for the bands formed from the eigenstates of  $\hat{H}'$ .

The optical coupling,  $\hat{V}'$ , is characterised by parameters  $\epsilon$  and  $\theta$  as well as the overall strength of the potential  $V$  (Appendix A). When  $\theta = \epsilon = 0$ , the optical potential does not couple the states  $g_+$  and  $g_-$ , and acts on each simply as a scalar potential, with the same symmetries as the hexagonal lattice discussed above when inversion symmetry is unbroken. The offsets of the momenta of  $g_{\pm}$  shift the Dirac points of these two states relative to each other. A small non-zero  $\theta$  breaks inversion symmetry and opens up gaps at the Dirac points in such a way that the pairs of bands are topologically trivial, i.e. have a net Chern number of zero. Non-zero  $\epsilon$  and  $\theta$  together break time-reversal symmetry and lead to bands with non-zero Chern number.

We have numerically calculated the bandstructure and Berry curvature of the lowest band for a case of large coupling, when  $V = 1.8E_R$ ,  $\theta = 0.3$  and  $\epsilon = 0.4$ , for which this band has Chern number of one (Figure 15). Note that in this case, the energy minimum of the band is not at  $\mathbf{k} = (0, 0)$ . Applying the force along  $(0, 1)$ , the

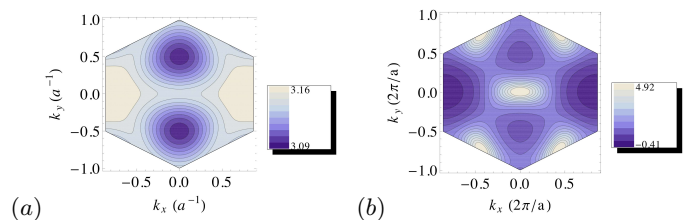


FIG. 15. (a) The energy (measured in  $E_R$ ) of the lowest band for  $V = 1.8E_R$ ,  $\theta = 0.3$  and  $\epsilon = 0.4$ . For these parameters, the lowest band has Chern number of one. (b) The corresponding Berry curvature.  $\Omega(\mathbf{k})$  is in units of  $1/[\text{BZ area}]$ . In this case, the Berry curvature is significant over much of the Brillouin zone and has regions of both positive and negative sign.

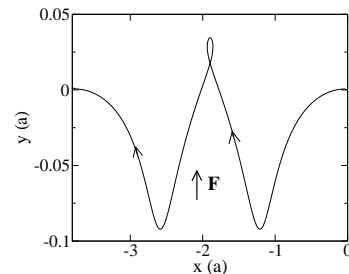


FIG. 16. The real space trajectory of a wavepacket under a force  $\mathbf{F} = (0.0, 1.0F_R)$  over one period, for  $V = 1.8E_R$ ,  $\theta = 0.3$  and  $\epsilon = 0.4$ . The wavepacket follows the path described in Figure 5. While the group velocity is again purely along  $y$ , the motion due to the Berry curvature is more complicated due to the varying sign of  $\Omega$ .

wavepacket will follow the same path as in the asymmetric hexagonal lattice (Figure 5). The resulting real-space trajectory is shown in Figure 16. Due to the simple alignment of the force, we can again associate the  $y$  motion with the group velocity and the  $x$  motion with the effects of the Berry curvature.

As the Berry curvature is substantially spread out through the Brillouin zone (Figure 15), there is now a continual drift along  $x$  over the trajectory. Since the Chern number is one, the Berry curvature is (largely) of the same sign along the trajectory, leading to a net drift of the wavepacket over one period of the Bloch oscillation. In this lattice, there are also regions of both positive and negative Berry curvature. When the Berry curvature is positive, the wavepacket travels in the negative  $x$  direction, while when  $\Omega$  is negative, the wavepacket moves along the positive  $x$  axis. The sign change will therefore not be detected if only the total drift is measured. Instead, the time-reversal procedure described above can again be applied to cleanly map out the local Berry curvature.

## VI. EXPERIMENTAL CONSIDERATIONS

We now consider how the velocity may be measured and how feasible it will be to observe the Berry curvature effects experimentally.

The mean atomic velocity may be extracted from the time-of-flight expansion image. This measures the momentum distribution[51], from which the mean momentum  $\langle \mathbf{p} \rangle$  may be deduced by the weighted average. The mean atomic velocity of the initial wavepacket then follows from Ehrenfest's theorem as  $\langle \mathbf{v} \rangle = \langle \mathbf{p} \rangle / m$ . This approach was successfully experimentally applied by Ben Dahan *et al.*[30] to detect Bloch oscillations in a one-dimensional lattice. The same approach applies for dressed states of internal atomic states, governed by (16); in this case the mean velocity can be obtained from the average momentum over all internal states.

Alternatively, it is possible to extract the velocity directly from measurements of the centre of mass motion in real-space. Thanks to recent experimental advances, the position of the wavepacket's centre of mass may be imaged with a high resolution, on the order of a lattice spacing [52]. For bands with nonzero Chern number, the Berry curvature can cause the wavepacket to have a net drift in space over each period of the Bloch oscillation; this leads to large cumulative effects on the position of the wavepacket over many oscillation periods. As described in Section IV A, measurements of the position of the wavepacket therefore offer a sensitive way to show that the Chern number of the band is nonzero. Indeed measurements of these drifting trajectories in constant applied force are equivalent to measurements of the *edge states* that must arise for a band with non-zero Chern number.

To this end, we consider how to maximise the importance of the effects of the Berry curvature relative to those of the group velocity. In the cases described above where the bands almost touch, we can consider the bandgap,  $\delta\varepsilon$ , as a small parameter. This applies to the hexagonal lattice when asymmetry is small and to the square one-photon optical flux lattice for small potential,  $V$ . (Note that the two-photon optical flux lattice is considered far from the band closing regime.) In the small bandgap limit, the momentum width,  $\delta k$ , over which the band is changed will be  $\delta k \simeq \delta\varepsilon / (\hbar v_R)$ , where  $v_R$  is the typical group velocity at the zone boundary for vanishing bandgap. The Berry curvature is therefore nonzero over the area,  $A \simeq (\delta k)^2$ . Assuming the Berry curvature is uniform within this, the invariance of the Chern number means  $\Omega \simeq 1/A \simeq 1/(\delta k)^2$ . The Berry velocity is  $\mathbf{v}_\Omega = (\dot{\mathbf{k}} \times \hat{\mathbf{z}})\Omega$  so, as the wavepacket traverses this region in one Bloch oscillation, the Berry curvature leads to a displacement of size  $\int v_\Omega dt \simeq \delta k \Omega \simeq 1/\delta k \simeq \hbar v_R / \delta\varepsilon$ . Conversely, the typical group velocity is  $\simeq v_R$  so over the period of one Bloch oscillation,  $\tau_B \simeq h/(Fa)$ , the typical amplitude of displacement is  $v_R \tau_B \simeq \hbar v_R / (Fa)$ . Thus, these contributions to the real-space trajectory have different dependences on  $\delta\varepsilon$ : the Berry curvature contri-

bution scales as  $1/\delta\varepsilon$ , while the contribution from the group velocity is independent of  $\delta\varepsilon$ . This is found in our numerical results, but is shown only qualitatively in the results presented in Figure 9, as in this case  $\delta\varepsilon$  is not that small. The effects of Berry curvature can therefore be maximised with respect to those of the group velocity by choosing a small bandgap. Note also that the two contributions have different dependences on the size of the force: the displacement due to the Berry curvature is independent of force, while that due to the group velocity is inversely proportional to it. Therefore, the Berry effects will be most evident for a high external force. Note, however, that there are some practical limitations. Too high a force is problematic as it increases the rate of Landau-Zener tunnelling, violating our assumption that the wavepacket remains in a single band. For small  $\delta\varepsilon$ , when the bands nearly touch, the Berry curvature becomes concentrated in small regions, of area  $(\delta k)^2$ . This then requires the momentum of the wavepacket and the alignment of the force to be precisely controlled in order to direct the wavepacket through this region. For intermediate bandgaps, the curvature is spread out. A natural compromise is to choose the bandgap such that  $\delta k$  is as small as the momentum uncertainty  $1/w$  with which a wavepacket can be prepared (here  $w$  is the spatial width of the wavepacket); one then expects the displacement due to the Berry curvature to be  $1/\delta k \simeq w$  on the order of the spatial extent of the wavepacket.

From our numerical calculations, we can quantitatively estimate the lengthscales of the dynamics. For example, we consider the dynamics of  $^{174}\text{Yb}$  atoms in the one-photon optical flux lattice, with  $\mathbf{F} = m\mathbf{g}$  along (1,1),  $\lambda = 578$  nm and  $V = 0.4E_R$ . The wavepacket follows the Brillouin zone path in Figure 9(a) and has a real-space trajectory similar to that of the solid line in Figure 9(b). As the wavepacket moves along section 1 of its path (from  $\mathbf{k} = (0, 0)$  to  $\mathbf{k} = (\pi/a, \pi/a)$ ), it moves with an average group velocity of  $2.2$  mm s $^{-1}$ , travelling approximately  $1.2$   $\mu\text{m}$  in the direction of the force in real-space. As it passes through  $\mathbf{k} = (\pi/a, \pi/a)$ , the wavepacket moves approximately  $1.3$   $\mu\text{m}$  perpendicular to the force due to the Berry curvature concentrated at this point. The group velocity then changes sign and the wavepacket travels  $1.2$   $\mu\text{m}$  in the opposite direction to the force (as it moves in the Brillouin zone from  $\mathbf{k} = (-\pi/a, \pi/a)$  to  $\mathbf{k} = (0, 2\pi/a)$ ). This behaviour repeats for sections 3 and 4 of its path. The average Berry velocity over one complete oscillation is therefore approximately  $1.1$  mm s $^{-1}$ . If the force is slightly misaligned, the trajectory will instead be a Lissajous-like oscillation, approximately bounded by a box of diagonal length  $1.2$   $\mu\text{m}$ . For the same Berry velocity, the wavepacket would then take approximately  $1.1$  ms to drift this distance. These length and time scales are within current experimental capabilities.

Two additional practical considerations are the effects of dispersion and interactions. The wavepacket will spread as it travels, and this dispersion could obscure

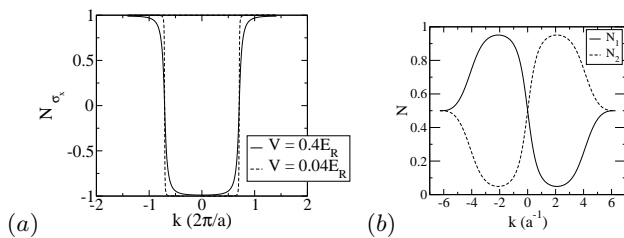


FIG. 17. (a) Oscillation in expectation value of  $\hat{\sigma}_x$  for the one-photon optical flux lattice, as the wavepacket travels along  $(1, 1)$ . The dashed line is for  $V = 0.04E_R$ , while the smooth line is  $V = 0.4E_R$ . The area over which the transfer occurs decreases with potential in a similar way to how the Berry curvature area decreases.  $k$  is measured along the path of the wavepacket. (b) Oscillation in population in the two states for the two-photon optical flux lattice as the wavepacket travels along  $(0, 1)$  for  $V = 1.8E_R$ ,  $\theta = 0.3$  and  $\epsilon = 0.4$ . The maximum population imbalance appear to be around points  $K$  and  $K'$ .  $k$  is measured along the path of the wavepacket.

the dynamics described. However, provided the centre of mass of the wavepacket can be measured to an accuracy greater than its width, this should not prevent the observation of Berry curvature effects.

Interactions destroy the coherence of a wavepacket over time and can have a strong dephasing effect on Bloch oscillations [31, 39, 53]. Nonlinearity can also lead to the collapse of the wavepacket into discrete solitons [53, 54]. We have ignored the effects of interactions in our analysis, an approximation suitable over these timescales for fermionic atoms [39], for species with low scattering lengths [41] or where the interaction strength can be tuned to zero by means of a Feshbach resonance [40, 55].

One can also look for distinct features in the momentum distributions of atoms undergoing Bloch oscillations in the optical flux lattices discussed above (Figure 17). In the two-photon optical flux lattice, the population of atoms oscillates between the two internal states as the wavepacket moves through the Brillouin zone. Near the points  $K$  and  $K'$ , the population imbalance is maximum but of opposite sign, reflecting the characteristics of the Berry curvature. In the one-photon optical flux lattice, the unfolding into the full magnetic Brillouin zone means the Bloch states are eigenstates of  $\hat{\sigma}_x$ . As a result, the oscillation takes place between those superpositions of the internal states that are eigenstates of  $\hat{\sigma}_x$  (and not between the internal states themselves). The transfer between eigenstates occurs over an area which decreases with potential, in a similar way to how the Berry curvature area decreases.

## VII. CONCLUSIONS

In summary, we have proposed a general method for mapping the local Berry curvature over the Brillouin zone in ultracold gas experiments. The Berry curvature crucially modifies the semiclassical dynamics and so affects

the Bloch oscillations of a wavepacket under a constant external force. In particular, the Berry curvature may lead to a net drift of the wavepacket with time. However, two-dimensional Bloch oscillations are interesting in their own right, and we may lose information about the Berry curvature due to the complicated Lissajous-like figures that may arise.

We have shown that this information can be recovered via a “time-reversal” protocol. The group velocity at a point in the Brillouin zone is invariant under a reversal of force, while the Berry velocity changes sign. As a result, the velocities under positive and negative force can be compared to extract either one or the other. This protocol will allow the local Berry curvature to be cleanly mapped out over the path of the wavepacket through the Brillouin zone.

We have demonstrated this protocol using the semiclassical dynamics of three model systems which are currently of experimental interest: the asymmetric honeycomb lattice and two optical flux lattices. Finally, we have discussed various experimental considerations, including how the velocity may be measured and how to maximise the magnitude of the Berry curvature effects on the dynamics. These methods can be used to characterise the topological character of bandstructures of complex optical lattices including optical flux lattices.

## ACKNOWLEDGMENTS

We are grateful to Tilman Esslinger for helpful conversations and to Eugene Demler for insightful comments on the importance of Ehrenfest’s theorem. This work was supported by the EPSRC.

### Appendix A: Hamiltonian for the Two-Photon Optical Flux Lattice for $F = 1/2$

The Hamiltonian acts in the  $g_{\pm}$  manifold, with the form of (16). The optical potential,  $\hat{V}(\mathbf{r})$ , is characterised by the Rabi frequencies  $\kappa_m$ ,  $m = 0, \pm 1$ , where  $m\hbar$  is the angular momentum along  $z$  gained by the atom when it absorbs a photon [17].

The potential is formed from laser beams at two frequencies:  $\omega_L$  and  $\omega_L + \delta$  where  $\delta$  is the Zeeman splitting of the ground states. The laser beams at  $\omega_L$  are linearly polarised and travelling in the  $xy$  plane, while the laser at  $\omega_L + \delta$  gives a plane wave propagating along the  $z$  axis with  $\sigma_z$  polarisation. The resulting potential takes the form:

$$\hat{V} = \frac{\hbar\kappa_{tot}^2}{3\Delta}\hat{1} + \frac{\hbar}{3\Delta} \begin{pmatrix} |\kappa_-|^2 - |\kappa_+|^2 & E\kappa_0 \\ E\kappa_0^* & |\kappa_+|^2 - |\kappa_-|^2 \end{pmatrix} \quad (\text{A1})$$

where  $\kappa_{tot}^2 = \sum_m |\kappa_m|^2$ ,  $\Delta = \omega_L - \omega_A$ , with  $\omega_A$  as the atomic resonance frequency and it is assumed that  $|\Delta| \gg$

$|\delta|, |\kappa_m|$ . The field of the laser at frequency  $\omega_L + \delta$  is characterised by  $E$ , which serves as a uniform, adjustable coupling.

The laser field at frequency  $\omega_L$  is formed from the superposition of three travelling plane waves of equal intensity and wavevectors  $\mathbf{k}_i$  in the  $xy$  plane. The setup discussed in Ref. 17 has triangular symmetry, with an angle of  $2\pi/3$  between the beams. The wavevectors are then  $\mathbf{k}_1 = -k/2(\sqrt{3}, 1, 0)$ ,  $\mathbf{k}_2 = k/2(\sqrt{3}, -1, 0)$  and  $\mathbf{k}_3 = k(0, 1, 0)$ . Up to a scale factor and rotation, this is the same geometry as the asymmetric hexagonal lattice in Section V A.

Each beam is linearly polarised at an angle  $\theta$  to the  $z$ -axis, giving

$$\kappa = \kappa \sum_{i=1}^3 e^{i\mathbf{k}_i \cdot \mathbf{r}} [\cos \theta \hat{\mathbf{z}} + \sin \theta (\hat{\mathbf{z}} \times \hat{\mathbf{k}}_i)], \quad (\text{A2})$$

where  $\kappa$  is the Rabi frequency of a single beam. The relative strength of the laser fields at frequencies  $\omega_L$  and  $\omega_L + \delta$  will henceforth be denoted as  $\epsilon = E/\kappa$ . The overall strength of the potential is  $V = \hbar^2 \kappa^2 / 3\Delta$ .

To define the unit cell, we consider a unitary transformation:  $\hat{U} \equiv \exp(-i\mathbf{k}_3 \cdot \mathbf{r} \hat{\sigma}_z / 2)$ . This gauge transformation is state dependent and leads to the Hamiltonian in Eqn. 20, where  $\hat{V}' = \hat{U}^\dagger \hat{V} \hat{U}$  has the same form as  $\hat{V}$ , with  $\kappa_0$  replaced by  $\kappa'_0 = e^{-i\mathbf{k}_3 \cdot \mathbf{r}} \kappa_0$ . The coupling then only includes the momentum transfers  $\mathbf{K}_{1,2} \equiv \mathbf{k}_{1,2} - \mathbf{k}_3$ . These define the reciprocal lattice vectors of the largest possible Brillouin zone, and the smallest possible real space unit cell. This unit cell is that of the hexagonal lattice discussed in Section V A.

- 
- [1] M. Z. Hasan and C. L. Kane, *Rev. Mod. Phys.* **82**, 3045 (2010)
- [2] X.-L. Qi and S.-C. Zhang, *Rev. Mod. Phys.* **83**, 1057 (2011)
- [3] D. J. Thouless, M. Kohmoto, M. P. Nightingale, and M. den Nijs, *Phys. Rev. Lett.* **49**, 405 (1982)
- [4] M. V. Berry, *Proc. R. Soc. London Ser. A* **392**, 45 (1984)
- [5] B. Simon, *Phys. Rev. Lett.* **51**, 2167 (1983)
- [6] M.-C. Chang and Q. Niu, *Phys. Rev. Lett.* **75**, 1348 (1995)
- [7] F. D. M. Haldane, *Phys. Rev. Lett.* **93**, 206602 (2004)
- [8] G.-B. Jo, J. Guzman, C. K. Thomas, P. Hosur, A. Vishwanath, and D. M. Stamper-Kurn, *ArXiv e-prints*(2011), arXiv:1109.1591
- [9] M. Aidelsburger, M. Atala, S. Nascimbène, S. Trotzky, Y.-A. Chen, and I. Bloch, *Phys. Rev. Lett.* **107**, 255301 (2011)
- [10] L. Tarruell, D. Greif, T. Uehlinger, G. Jotzu, and T. Esslinger, *ArXiv e-prints*(2011), arXiv:1111.5020
- [11] D. Jaksch and P. Zoller, *New Journal of Physics* **5**, 56 (2003)
- [12] E. J. Mueller, *Phys. Rev. A* **70**, 041603 (2004)
- [13] A. S. Sorensen, E. Demler, and M. D. Lukin, *Phys. Rev. Lett.* **94**, 086803 (2005)
- [14] F. Gerbier and J. Dalibard, *New Journal of Physics* **12**, 033007 (2010)
- [15] J. Dalibard, F. Gerbier, G. Juzeliūnas, and P. Öhberg, *Rev. Mod. Phys.* **83**, 1523 (2011)
- [16] N. R. Cooper, *Phys. Rev. Lett.* **106**, 175301 (2011)
- [17] N. R. Cooper and J. Dalibard, *EPL* **95**, 66004 (2011)
- [18] M. Kohmoto, *Annals of Physics* **160**, 343 (1985), ISSN 0003-4916
- [19] K. Novoselov, A. Geim, S. Morozov, D. Jiang, M. Katsnelson, I. Grigorieva, S. Dubonos, and A. Firsov, *Nature* **438**, 197 (2005)
- [20] Y. Zhang, Y. Tan, H. Stormer, and P. Kim, *Nature* **438**, 201 (2005)
- [21] Y. Liu, G. Bian, T. Miller, and T.-C. Chiang, *Phys. Rev. Lett.* **107**, 166803 (2011)
- [22] D. Xiao, M.-C. Chang, and Q. Niu, *Rev. Mod. Phys.* **82**, 1959 (2010)
- [23] T. Jungwirth, Q. Niu, and A. H. MacDonald, *Phys. Rev. Lett.* **88**, 207208 (2002)
- [24] M. Onoda and N. Nagaosa, *Journal of the Physical Society of Japan* **71**, 19 (2002)
- [25] M.-C. Chang and Q. Niu, *Phys. Rev. B* **53**, 7010 (1996)
- [26] G. Sundaram and Q. Niu, *Phys. Rev. B* **59**, 14915 (1999)
- [27] E. Zhao, N. Bray-Ali, C. J. Williams, I. B. Spielman, and I. I. Satija, *Phys. Rev. A* **84**, 063629 (2011)
- [28] E. Alba, X. Fernandez-Gonzalvo, J. Mur-Petit, J. K. Pachos, and J. J. Garcia-Ripoll, *Phys. Rev. Lett.* **107**, 235301 (2011)
- [29] J. Feldmann, K. Leo, J. Shah, D. A. B. Miller, J. E. Cunningham, T. Meier, G. von Plessen, A. Schulze, P. Thomas, and S. Schmitt-Rink, *Phys. Rev. B* **46**, 7252 (1992)
- [30] M. Ben Dahan, E. Peik, J. Reichel, Y. Castin, and C. Salomon, *Phys. Rev. Lett.* **76**, 4508 (1996)
- [31] B. P. Anderson and M. A. Kasevich, *Science* **282**, 1686 (1998)
- [32] A. M. Dudarev, R. B. Diener, I. Carusotto, and Q. Niu, *Phys. Rev. Lett.* **92**, 153005 (2004)
- [33] R. B. Diener, A. M. Dudarev, G. Sundaram, and Q. Niu, *ArXiv e-prints*(2003), arXiv:1111.5020
- [34] A. R. Kolovsky and H. J. Korsch, *Phys. Rev. A* **67**, 063601 (2003)
- [35] D. Witthaut, F. Keck, H. J. Korsch, and S. Mossmann, *New Journal of Physics* **6**, 41 (2004)
- [36] S. Mossmann, A. Schulze, D. Witthaut, and H. J. Korsch, *Journal of Physics A: Mathematical and General* **38**, 3381 (2005)
- [37] N. W. Ashcroft and D. N. Mermin, *Solid State Physics* (Thomson Learning, Toronto, 1976)
- [38] C. F. Bharucha, K. W. Madison, P. R. Morrow, S. R. Wilkinson, B. Sundaram, and M. G. Raizen, *Phys. Rev. A* **55**, R857 (1997)
- [39] G. Roati, E. de Mirandes, F. Ferlaino, H. Ott, G. Modugno, and M. Inguscio, *Phys. Rev. Lett.* **92**, 230402 (2004)
- [40] M. Fattori, C. D'Errico, G. Roati, M. Zaccanti, M. Jonas-Lasinio, M. Modugno, M. Inguscio, and G. Modugno, *Phys. Rev. Lett.* **100**, 080405 (2008)

- [41] G. Ferrari, N. Poli, F. Sorrentino, and G. M. Tino, Phys. Rev. Lett. **97**, 060402 (2006)
- [42] A. R. Kolovsky and G. Mantica, Phys. Rev. E **83**, 041123 (2011)
- [43] A. R. Kolovsky, ArXiv e-prints(2011), arXiv:1106.0945
- [44] T. Fukui, Y. Hatsugai, and H. Suzuki, Journal of the Physical Society of Japan **74**, 1674 (2005)
- [45] J. M. Zhang and W. M. Liu, Phys. Rev. A **82**, 025602 (2010)
- [46] G. W. Semenoff, Phys. Rev. Lett. **53**, 2449 (1984)
- [47] P. Soltan-Panahi, J. Struck, P. Hauke, A. Bick, W. Plenkers, G. Meineke, C. Becker, P. Windpassinger, M. Lewenstein, and K. Sengstock, Nat Phys **7**, 434 (2011)
- [48] F. D. M. Haldane, Phys. Rev. Lett. **61**, 2015 (1988)
- [49] S. Y. Zhou, G.-H. Gweon, A. V. Fedorov, P. N. First, W. A. De Heer, D.-H. Lee, F. Guinea, A. H. C. Neto, and A. Lanzara, Nature Materials **6**, 770 (2007)
- [50] D. Xiao, W. Yao, and Q. Niu, Phys. Rev. Lett. **99**, 236809 (2007)
- [51] I. Bloch, J. Dalibard, and W. Zwerger, Rev. Mod. Phys. **80**, 885 (2008)
- [52] T. Esslinger, Private Communication
- [53] A. Trombettoni and A. Smerzi, Phys. Rev. Lett. **86**, 2353 (2001)
- [54] A. M. Dudarev, R. B. Diener, and Q. Niu, Journal of Optics B: Quantum and Semiclassical Optics **6**, S231 (2004)
- [55] M. Gustavsson, E. Haller, M. J. Mark, J. G. Danzl, G. Rojas-Kopeinig, and H.-C. Nägerl, Phys. Rev. Lett. **100**, 080404 (2008)